Electronic Supplementary Material (ESI) for ChemComm.

Supporting Information

Partially Sulfurized NiMn-ZIF with High Stability for Aqueous Nickel-Zinc Batteries

Yiluo Tian[a], Yichun Su[a], Qian Li[a], Wanchang Feng[a], Meifang Yang[a], Zheng Liu[a], Huan Pang*[a,b]*

[a]School of Chemistry and Chemical Engineering, Yangzhou University, Yangzhou, 225009, P. R. China

[b]State Key Laboratory of Coordination Chemistry, Nanjing University, Nanjing, Jiangsu, 210023, P. R. China

*Corresponding author. Email: liuzhengbeyond@163.com (Zheng Liu)

huanpangchem@hotmail.com; panghuan@yzu.edu.cn (H. Pang)

Content

1.Experimental Section

1.1 Preparation of Ni-ZIF-X(X=0.5, 0.05, 1, 2, 3, 4).

Ni-ZIF-X was obtained following similar process in previous reports with some modifications[1]. Prior to synthesis, A solution of 500 ml DMF of 29.6327g nickel nitrate hexahydrate was prepared (A), and an amount of 2-methylimidazole was dissolved in 25 ml DMF (B). 10ml of solution A was slowly dripped into 25ml of solution B, stirring while dripping. After stirring for ten minutes, the mixture was transferred to a 50 ml Teflon-lined stainless-steel autoclave and kept at 160 ° C for 12 h. After cooling to room temperature, the products were washed repeatedly with DMF. Finally, Ni-ZIF was obtained after drying the product in a vacuum drying oven at 80 ° C overnight.

1.2 Preparation of NiM-ZIF (M = Ag^{+}, Mn^{2+}, Cu^{2+}, Zn^{2+}, Al^{3+}, Fe^{3+}).

To modulate the electronic structure, different metal cations (M= Ag^{+}, Mn^{2+}, Cu^{2+}, Zn^{2+}, Al^{3+}, Fe^{3+}) are introduced into the Ni-ZIF through one-pot hydrothermal method. Based on the different crystal structure of composites after another metal ions doping, the intermediates of NiM-ZIF (M=, Mn^{2+}, Cu^{2+}, Zn^{2+}) and Ni-ZIF-M (M=Ag^{+}, Al^{3+}, Fe^{3+}) are respectively synthesized. It should be noted that because of the excessive redox properties and poor coordination capability of Ag^{+}, Al^{3+} and Fe^{3+}, the original ZIF skeleton is destroyed, and the corresponding new compounds are formed.

The synthesis method of NiM-ZIF is roughly the same as that of Ni-ZIF-X, except that a certain amount of $M_x(NO_3)_2 \cdot nH_2O$ (Ag^{+}、Mn^{2+}、Cu^{2+}、Zn^{2+}、Al^{3+}、Fe^{3+}) is added to the solution.

1.3 Preparation of NiMn-ZIF-Sx (x=1, 2, 3, 4, 5, 6)

To obtain the partial sulphuration of the material, the NiMn-ZIF was used as an example and the black NiMn-ZIF-Sx was finally prepared by hydrothermal reaction with different proportions of thioacetamide at 120 °C for 4 h (x is the thioacetamide to sample mass ratio). The products were all blackened despite the different proportions of the sulfur source. The preparation of NiMn-ZIF-Sx was synthetically referenced to previous work with some adjustments[2]. 20mg of NiMn-ZIF sample and a

certain amount of thioacetamide were dispersed in 40ml of ethanol, stirred for ten minutes, and then transferred to a 50 ml Teflon-lined stainless-steel autoclave and maintained at 120 ℃ for four hours. After cooling to room temperature, the products were washed repeatedly with ethanol. Finally, NiMn-ZIF-Sx was obtained after drying the product in a vacuum drying oven at 60 ℃ overnight.

1.4 Material characterization

All chemicals, $AgNO_3$, $Cu(NO_3)_2{\cdot}3H_2O$, including $Ni(NO_3)_2{\cdot}6H_2O$, $Zn(NO_3)_2{\cdot}6H_2O$, $Al(NO_3)_3{\cdot}9H_2O$, $Mn(NO_3)_2{\cdot}4H_2O$, $Fe(NO_3)_3{\cdot}9H_2O$, 2-methylimidazole, N,N-dimethylformamide (DMF) and ethanol were purchased from Shanghai Sinopharm Chemical Reagent and used without further treatment or purification. All aqueous solutions were prepared with high-purity de-ionized water (DI water, resistance 18 MΩ cm^{-1}).

A scanning electron microscope (SEM, Zeiss_Supra55) was used for observing the morphology of the samples and energy dispersive X-ray (EDS) spectroscopy at an acceleration voltage of 5.0 kV and 20.0 kV, respectively. The products were tested by X-ray diffraction (XRD) on a Bruker D8 Advanced X-ray Diffractometer (Cu-Kα radiation: λ = 0.15406 nm) for phase analysis and compared to the simulated diffraction pattern of Ni-MOF-74 taken from reference 3. In situ XRD were used to analysis the mechanism of the electrodes during charge/discharge cycles on X-ray diffractometer (MiniFlex600-C). Fourier Transform Infrared Spectroscopy (FTIR) measurement was performed on a TENSOR27. The products were tested by Raman on a DXRxi Raman Imaging Microscope for functional group analysis. ICP-OES measurements were performed using a simultaneous ICP spectrometer (model Optima 7300 DV; PerkinElmer Inc., USA) equipped with a solid-state detector. Samples were dissolved using aqua regia, and then dilute for test. X-ray photoelectron spectroscopy (XPS) was carried out on a Thermo Scientic ESCALAB 250 apparatus. Transmission electron microscopy (TEM) images, High-resolution transmission electron microscopy (HRTEM) images, selected area electron diffraction (SAED) images, high-angle annular dark-feld scanning TEM (HAADF-STEM) and energy dispersive X-ray spectroscopy mapping were captured on a Tecnai G2 F30 transmission electron microscope at an acceleration voltage of 300 kV. Brunauer-Emmett-Teller (BET) and Barrett-Joyner-Halenda (BJH) were carried out on Autosorb IQ3. In addition, all electrochemical measurements were

carried out by using a CHI 660E instrument. The XAFS data were background subtracted from the overall absorption, normalized, and Fourier transformed by standard procedures within the Athena program. X-ray absorption structure (XAFS) measurements at the Co and Ni K-edge were carried out on Shanghai Light Source (SSRF, BL14W1). The SSRF is composed of a 150 MeV linear accelerator, a 3.5 GeV booster, a 3.5 GeV storage ring, beamlines and experimental stations. The obtained XAFS data were processed in Athena (version 0.9.26) for background, pre-edge line and post-edge line calibrations. Then Fourier transformed fitting was carried out in Artemis (version 0.9.26).

1.5 Preparation of Ni-ZIF-X, NiM-ZIF and NiMn-ZIF-Sx electrodes. (X=0.05, 0.5, 1, 2, 3, 4, x=1, 2, 3, 4, 5, 6)

Prior to the preparation, the carbon cloth (CC) was first ultrasonically cleaned in acetone, absolute ethanol and DI water alternately for 3 - 4 times for 30 min each time. Then, the treated CC was placed in a vacuum drying oven to be dried at 60°C overnight. To fabricate the working electrodes, active materials, acetylene black, and polyvinylidene difluoride (PVDF) were well mixed in a weight ratio of 8:1:1 in N-methyl pyrrolidone (NMP). Then, the formed slurry was sonicated for 30 min before depositing on a 1 cm × 2 cm CC, ensuring samples coated within 1 cm × 1 cm. The typical mass loading of the active material was about 2.4 mg cm^{-2}. Finally, Ni-ZIF-X@CC, NiM-ZIF@CC and NiMn-ZIF-Sx@CC electrodes were acquired after drying overnight at 60 °C in a vacuum drying oven.

1.6 Electrochemical measurements.

Electrochemical measurements of Ni-ZIF-X@CC, NiM-ZIF@CC and NiMn-ZIF-Sx@CC electrodes (1 x 1 cm^2) were carried out in a three-electrode system in an aqueous electrolyte of KOH (3 M) using an electrochemical workstation (CHI 660E). The AC frequency ranged from 0.01 to 10^5 Hz with an amplitude of 5 mV. A Pt wire was used as the counter electrode and a Hg/HgO electrode was the reference electrode. Electrochemical measurements of nickel-zinc batteries were performed in a two-electrode system with 3 M KOH + 20 mM zinc acetate ($Zn(Ac)_2$) as the electrolyte. The Ni-ZIF-X@CC, NiM-ZIF@CC and NiMn-ZIF-Sx@CC electrodes (1 x 2 cm^2) were the cathode and Zn (1 x 2 cm^2) was the anode. 10 cycles of electrochemical activation process were carried out before

electrochemical testing. All current densities are based on the mass of active materials on the CC.

Calculations

The areal specific capacity C_A (mA h cm^{-2}) of the electrodes in three-electrode system were calculated from discharging curves according the following equation:

$$C_A = \frac{I \times \Delta t}{S}$$

where I (mA) is the discharging current, t (h) is the discharging time, and (cm^2) is the area of the electrodes (1 cm^2).

Alternatively, the areal specific capacity of the NZBs (C_{cell}) in two-electrode system was calculated from the discharging curves according the following equation:

$$C_{cell} = \frac{I \times \Delta t}{S}$$

where C_{cell} (mAh cm^{-2}) is the areal specific capacity of the NZBs, I (mA) is the discharging current, t (h) is the discharging time, and (cm^2) is the total surface area of the NZBs (1 cm^2).

The areal energy density (E) and areal power density (P) of the battery were calculated from the following equations:

$$E = \frac{I \int_0^{\Delta t} U(t)dt}{S}$$

$$P = \frac{E}{\Delta t}$$

where E (mWh cm^{-2}) is the areal energy density, I(mA) is the discharging current, U(t) is the votage during discharge (V), dt is the time differentia, t(h) is the discharging time, and (cm^2) is the total surface area of the NZBs (1 cm^2). P (mW cm^{-2}) is the areal power density and t(h) is the discharging time.

To obtain the partial sulphuration of the material, the NiMn-ZIF was used as an example and the black NiMn-ZIF-Sx was finally prepared by hydrothermal reaction with different proportions of thioacetamide at 120 °C for 4 h (x is the thioacetamide to sample mass ratio). The products were all blackened despite the different proportions of the sulfur source.

Particularly, when the mass of thioacetamide added is half of the mass of nickel nitrate hexahydrate, the sample is noted as NiMn-ZIF-S1.

2 SEM diagram of Ni-ZIF-X

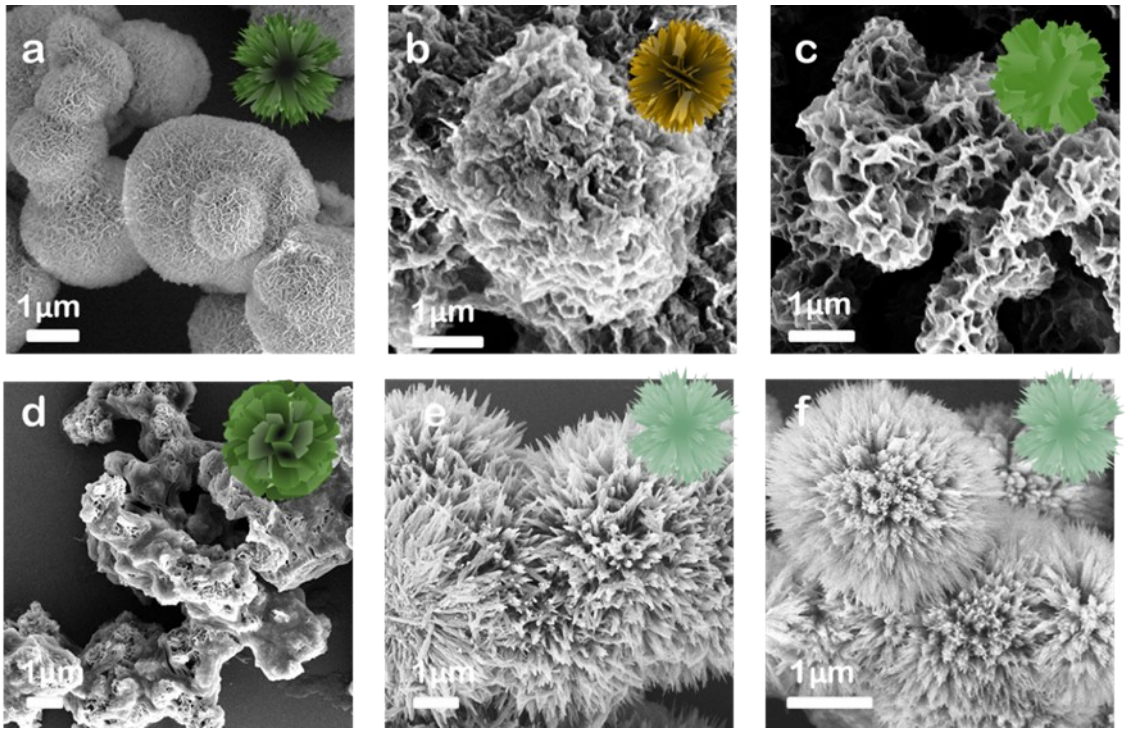

Figure S1. SEM diagram of Ni-ZIF-X, (a)0.05:1(ligand: metal), (b)0.5:1, (c)1:1, (d)2:1, (e)3:1, (f)4:1.

3 SEM diagram of incorporation of different metals NiM-ZIF

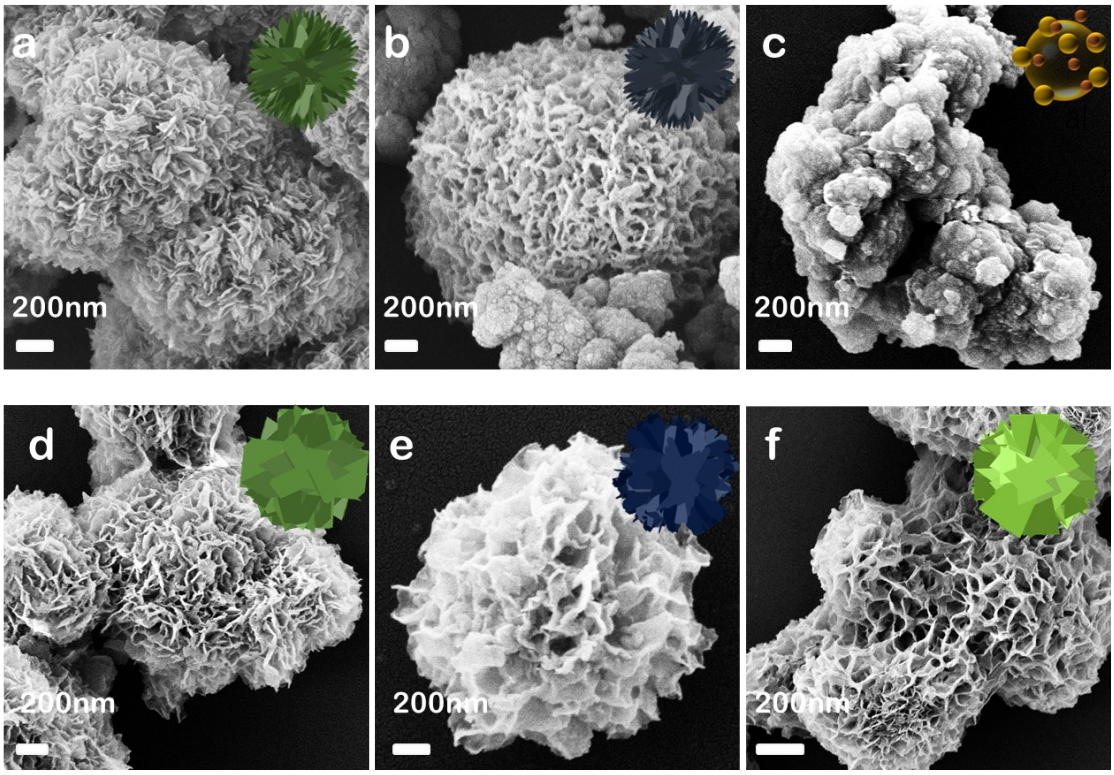

Figure S2. SEM diagram of incorporation of different metals NiM-ZIF: (a)NiMn-ZIF; (b)Ni-ZIF-Ag; (c)Ni-ZIF-Al; (d)NiZn -ZIF; (e)Ni-ZIF-Fe; (f)NiCu-ZIF.

4. SEM diagram of NiMn-ZIF-Sx

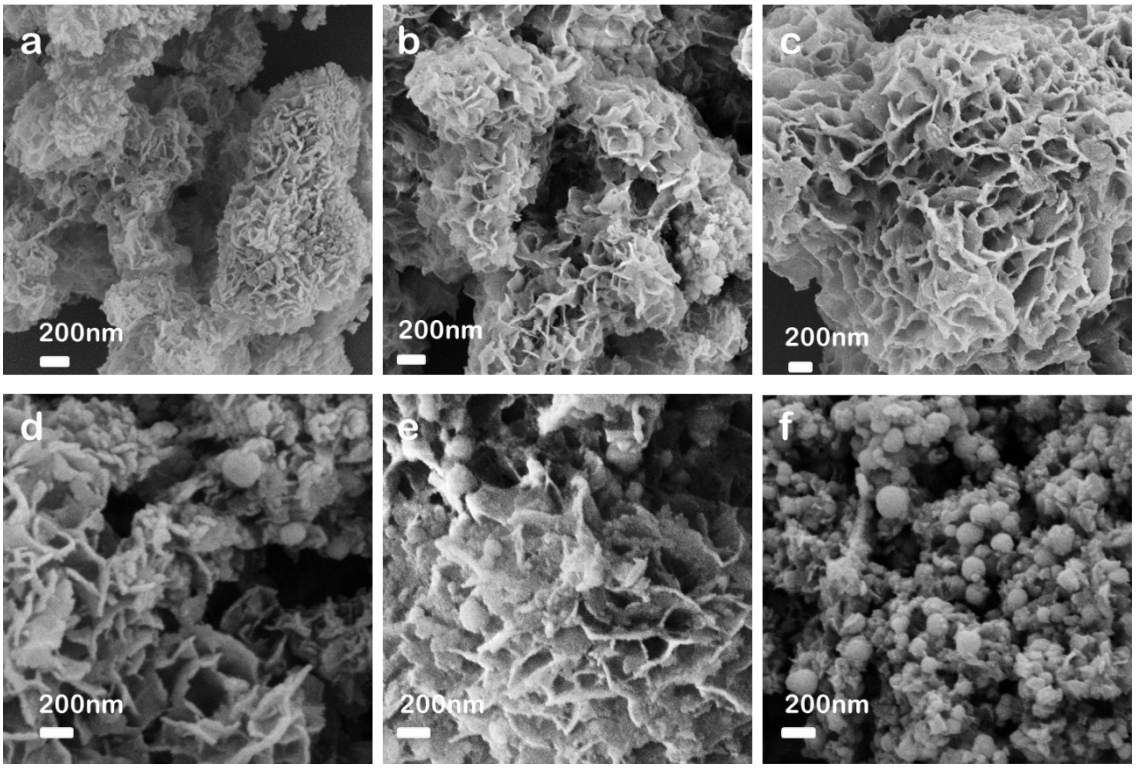

Figure S3. SEM diagram of NiMn-ZIF-Sx: (a)NiMn-ZIF-S1; (b)NiMn-ZIF-S2; (c)NiMn-ZIF-S3; (d)NiMn-ZIF-S4; (e)NiMn-ZIF-S5; (f)NiMn-ZIF-S6.

5. SEM images and corresponding energy-dispersive spectroscopy (EDS) mapping images of NiM-ZIF.

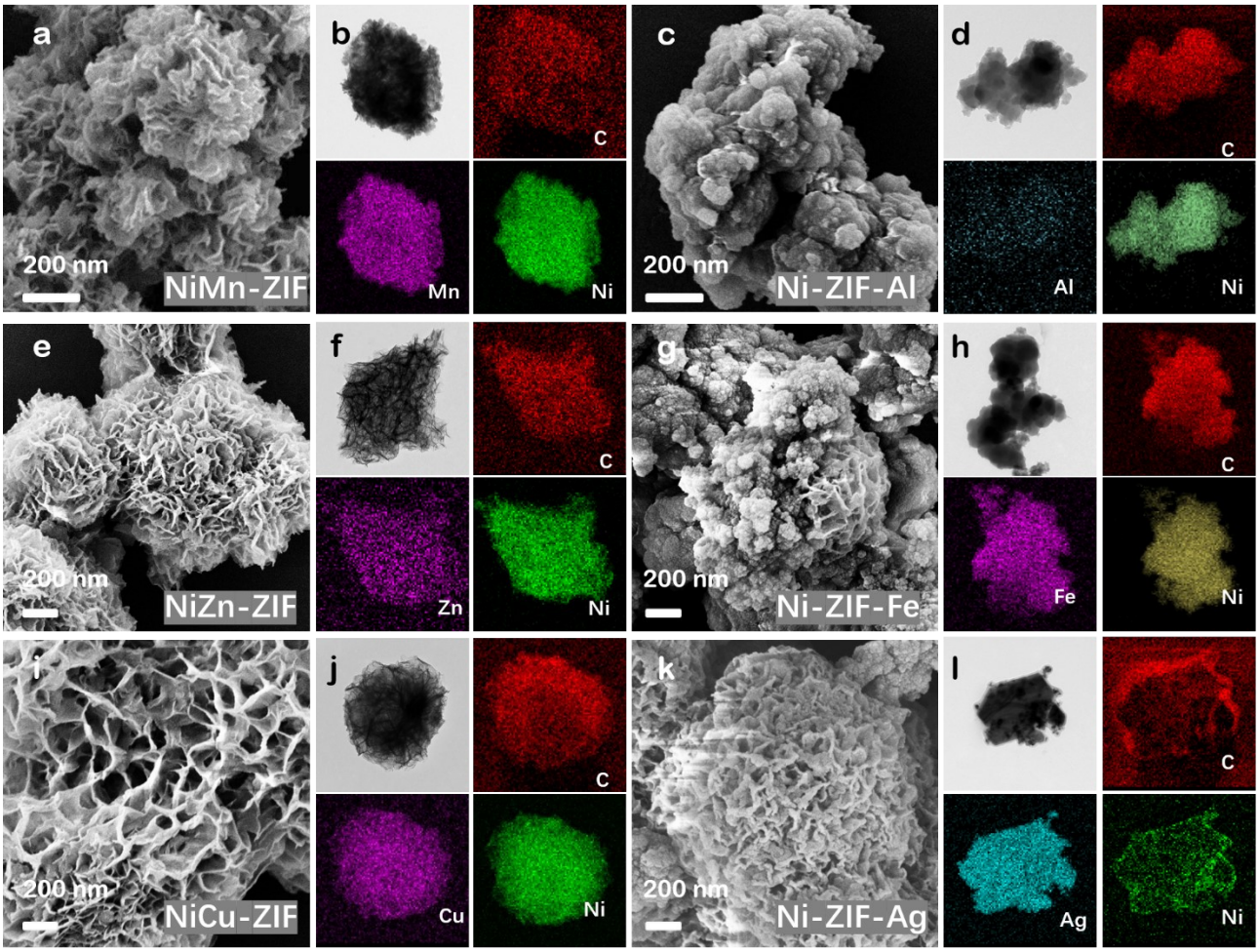

Figure S4. (a-l) SEM images and corresponding energy-dispersive spectroscopy (EDS) mapping images of NiMn-ZIF (a, b), Ni-ZIF-Al (c, d), NiZn-ZIF (e, f), Ni-ZIF-Fe (h, i), NiCu-ZIF (i, j), and Ni-ZIF-Ag (k, l).

The corresponding mapping shows a uniform distribution of Ni and M, except for silver. The doped metal ions were successfully and uniformly distributed on the skeleton. Similarly, due to the over competition of dopant ions, it can be found that the three samples, Ni-ZIF-Al, Ni-ZIF-Fe, and Ni-ZIF-Ag, contain less nickel ions.

6. **SAED pattern of the NiMn-ZIF-S5**

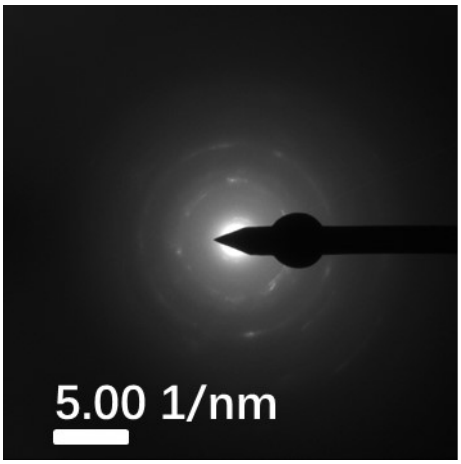

Figure S5. SAED pattern of the NiMn-ZIF-S5.

7. **XRD spectra of different samples**

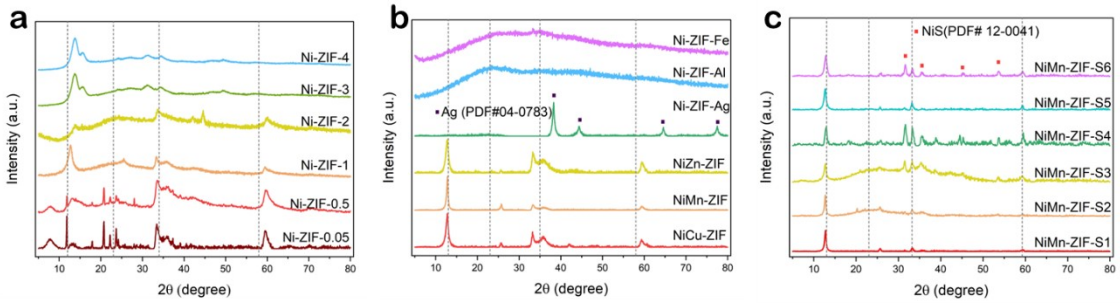

Figure S6. XRD spectra of different samples.

After the addition of Al^{3+}, Fe^{3+}, and Ag^{+}, the sharp peaks of the precursor completely disappeared. And the former two samples were in the amorphous state, while several strong diffraction peaks of the latter were consistent with that of silver (PDF#04-0783), and the original ZIF skeleton had been completely transformed. The samples doped with silver ions were completely converted to silver monomers, which may be related to the strong reducing properties of silver due to its high redox potential. The difference of XRD spectra after the addition of Cu^{2+}, Zn^{2+}, and Mn^{2+} is very small, indicating that the precursor skeleton is stable after the addition of the above three ions.

The observed discrepancy in XRD patterns is hypothesized to be associated with the valence states of the doped ions. Trivalent ions, differing in ionic radius and coordination requirements from the divalent nickel ions, may induce lattice distortions or structural disorder, potentially leading to amorphization[3]. In contrast, the incorporation of divalent ions exerts a comparatively minor perturbation on charge equilibrium and crystal structure, thereby facilitating the preservation of the original crystalline order[4].

8. FT-IR spectra of Ni-ZIF-X samples

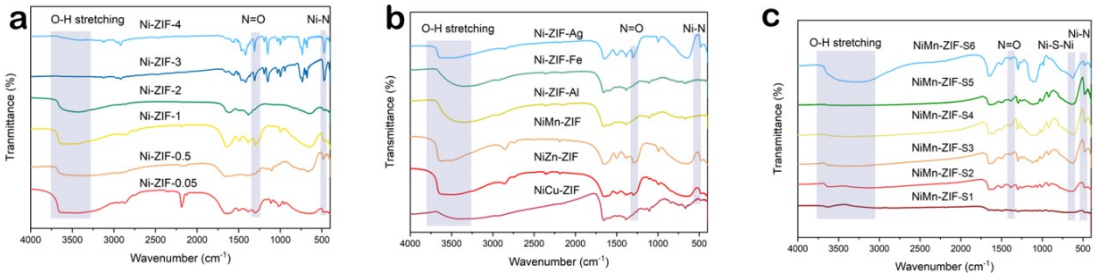

Figure S7. FT-IR spectra of different samples.

Trace amounts of metal doping did not disrupt these skeletons(Fig. S7b) It can be observed that the vibration peak assigning to Ni–S–Ni becomes progressively stronger at 654 cm^{-1} with increasing the sulfidation degree (Fig. S7c), further indicating that the spheres attached to the Ni-ZIF nanosheets are nickel sulfide[5].

9.BET

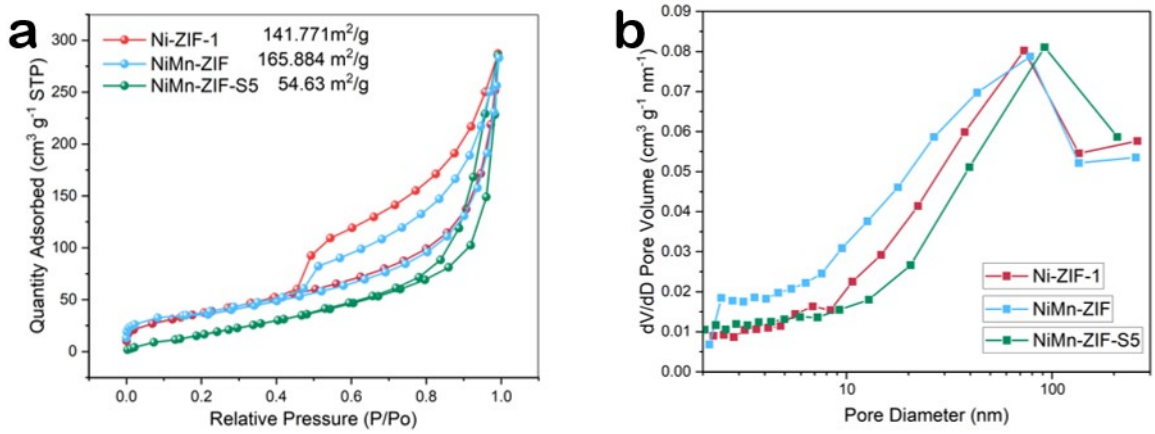

Figure S8. N2 adsorption-desorption isotherms at 77 K spectra and Pore size distribution plots of different samples.

It can be seen that the former two behave as type IV adsorption isotherms with hysteresis lines between P/P_0 = 0.4 ~ 1.0 with a bias towards medium pressure, indicating the presence of a mesoporous structure in the composites[6] (Fig. S8a). The latter is a type III adsorption isotherm with hysteresis between P/P_0 = 0.8 ~ 1.0, and the curve is concave because the interactions between adsorbate molecules are stronger than those between adsorbate and adsorbent[7]. Videlicet, the sulfide sample is less adsorbent than the former two. The BET surface areas of Ni-ZIF-1, NiMn-ZIF and NiMn-ZIF-S5 are calculated to be 165.88, 141.77 and 54.63 m^2g^{-1}, respectively (Table S2). It is associated with the fact that the metal sulfuretted formed by sulfation cover the ZIF surface inhibiting the exposure of the ZIF active sites[8]. Although the sulfation is inevitably to ruin the porous structures of ZIF, the destroy tendency is effectively attenuated by partial sulfation[9]. Besides, pore size distribution of Ni-ZIF-1, NiMn-ZIF and NiMn-ZIF-S5 was calculated by the Barrett Joyner-Halenda methods (Fig. S8b). This further supports the gain of metal doping on pore size enlargement.

10.XPS spectra

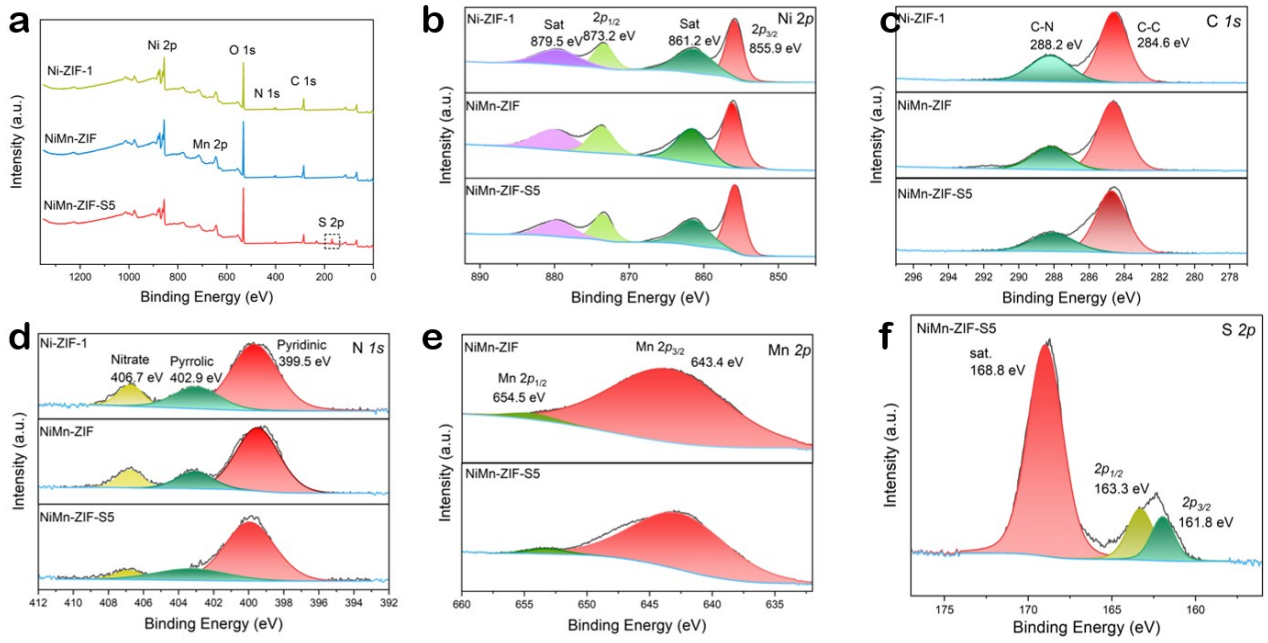

Figure S9. XPS spectra of the Ni-ZIF-1, NiMn-ZIF and NiMn-ZIF-S5.

From Fig. S9c, it can be seen that the C 1s spectrum is separated into two peaks consisting of a C–C bond at 284.6 eV and a C–N bond at 288.2 eV from the organic linker 2-methylimidazole[1]. Similarly, the high-resolution N 1s spectra of the three materials were split into three peaks, as shown in Fig. S9d. There are three peaks situated in binding energies: 406.7 eV, 402.9 eV, and 399.5 eV, which are characteristic of Nitrate (406.7 eV), Nitrogen (402.9 eV), and Pyridinic nitrogen (399 eV)[1]. The above-mentioned results prove the successful construction of the partially sulfurized NiMn-ZIF-S5 while retaining Ni-ZIF skeleton. Fig. S9e shows the Mn 2p profile, $2p_{1/2}$ and $2p_{2/3}$ appear at 654.5 eV and 643.4 eV, with a spin energy separation of 11.1 eV, indicating that manganese ions are demonstrated in the sample in the +2 valence state[10]. The S 2p spectrum reveals two distinct $2p_{1/2}$ and $2p_{3/2}$ peaks at 163.8 eV and 161.1 eV (Fig. S9f), suggesting the presence of negative divalent sulfur ions in the sulfuretted composites[11].

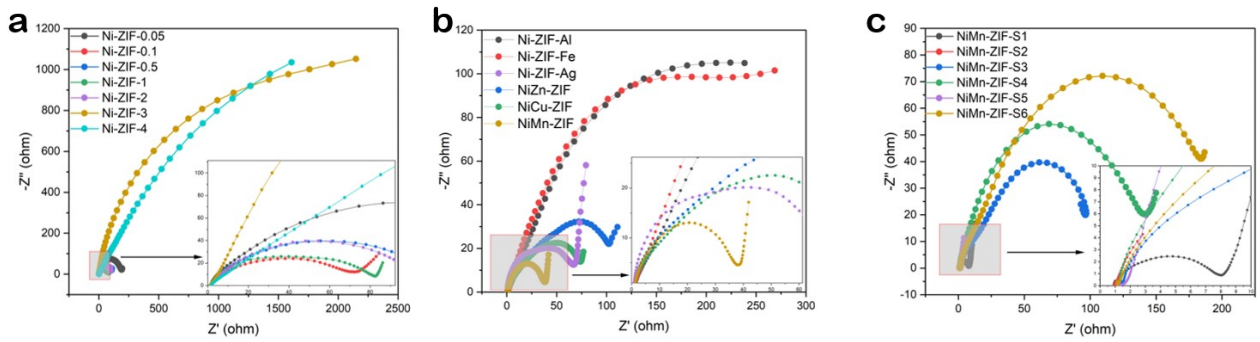

11. the EIS spectra of different samples

Figure S10. the EIS spectra of different samples :(a) Ni-ZIF-X, (b) NiM-ZIF, and (c) Ni-ZIF-Sx.

An overview of the capacitive and resistive properties of the electrode materials is presented using electrochemical impedance spectroscopy (EIS). EIS is the major analytical method for studying the charge transfer properties of electrodes and electrolyte surfaces. The Nyquist diagram can be used to understand the charge transfer resistance. The Nyquist plots of the test electrodes are usually in the frequency range of 0.01-10^5 Hz and are divided into two regions according to the frequency level: the region of high-frequency and the region of low-frequency. The former is usually a semicircle and the latter a straight line as shown in Fig. S10. Two important parameters that are closely related to the capacitance and resistance characteristics of the battery, the equivalent series resistance (Rs) charge transfer resistance (R_{ct}), can be obtained from the graph. The differential between the start and end points of the semicircle is related to the R_{ct} value, and the semicircle starts with the Rs value, which includes the contact resistance at the active material/collector interface, the intrinsic resistance of the active material, and the electrolyte solution resistance[11, 12]. The Rs values of the Ni-ZIF-1, NiMn-ZIF and NiMn-ZIF-S5 electrodes are as small as 2.01, 1.29 and 1.24 Ω, respectively, which are corresponded to the low resistance of the electrodes in the electrolytic solution. The charge transfer kinetics, which occurs at the electrode-electrolyte interface, is related to Rs. The NiMn-ZIF-S5 electrode has the smallest value of Rs, indicating that it has higher charge transfer kinetics than the first two samples. Also, after metal doping

and sulfidation, there is a very significant and substantial reduction in R_{ct}, demonstrating that the ion flow pathway is not blocked and the charge/discharge time is improved. The slope of the straight line in the low-frequency region was used to read the Warburg diffusion resistance (Zw), which is caused by the diffusion of electrolyte ions into the electrode. It is evident from Fig. 5i that the slope of the NiMn-ZIF-S5 electrode is larger than the Ni-ZIF-1 and NiMn-ZIF electrodes, which is an indication of a faster transport process of electrolyte ions to the electrode surface, explaining why the NiMn-ZIF-S5 composite has a good rate capability[11].

12. Electrochemical performance of aqueous Ni-ZIF-1//Zn and NiMn-ZIF//Zn battery

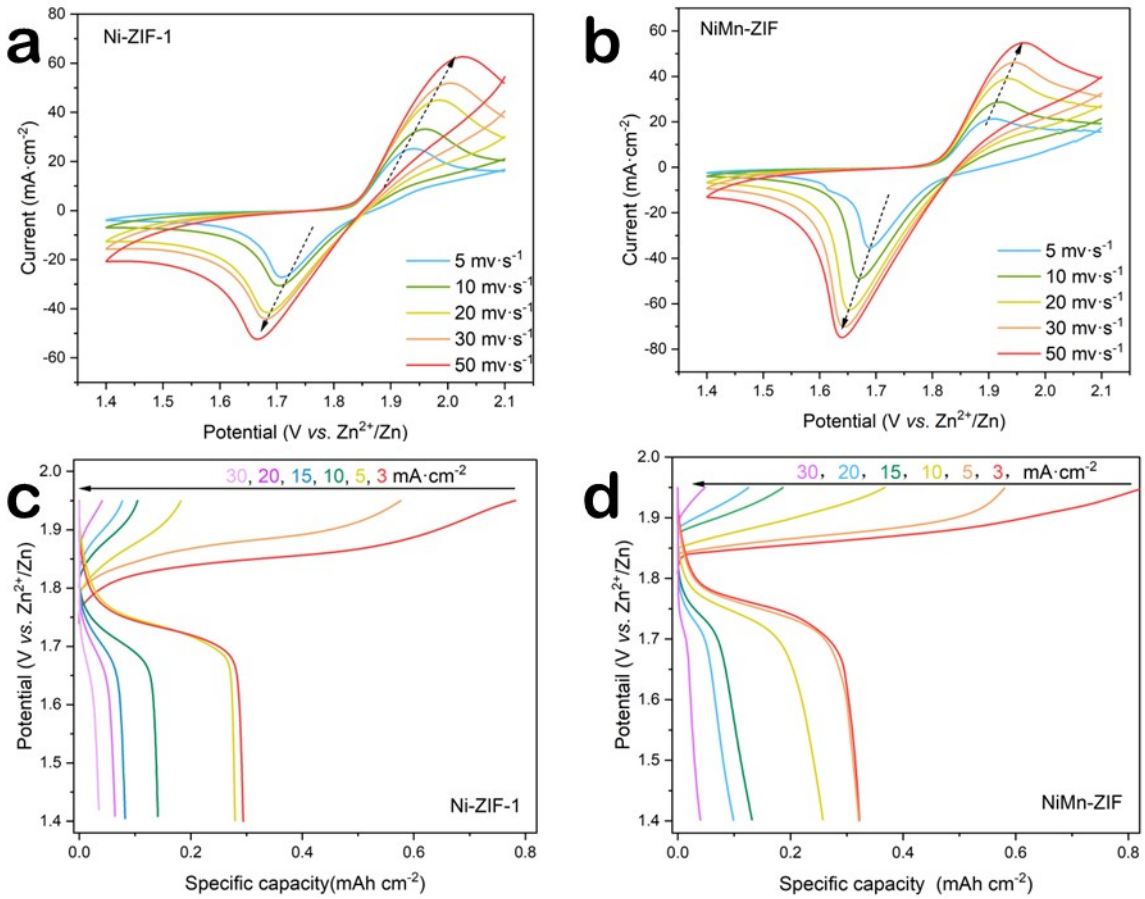

Figure S11. Electrochemical performance of aqueous Ni-ZIF-1//Zn and NiMn-ZIF//Zn battery. (a, b) CV curves at different scan rates. (c, d) GCD curves at various specific currents.

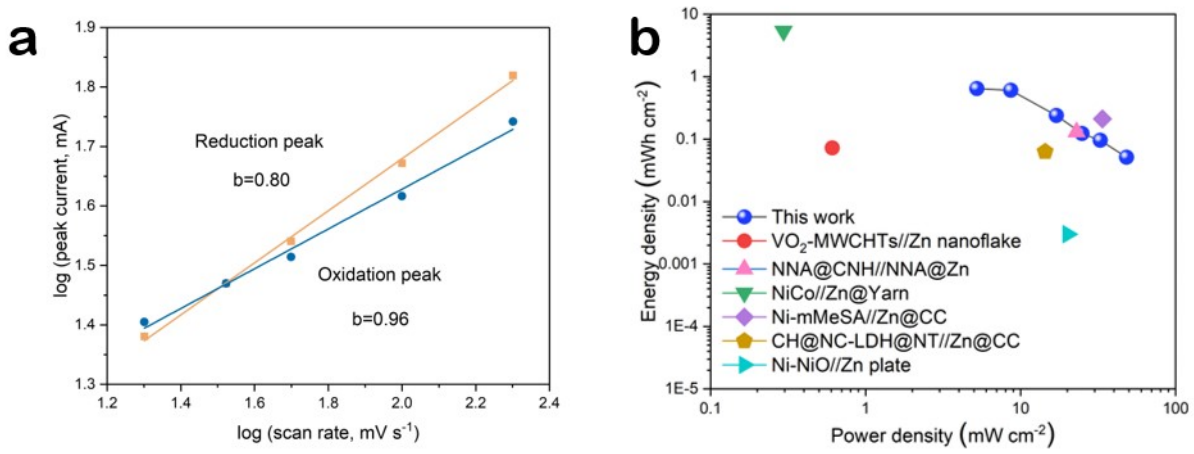

13. Plots of log (i) vs log (v) of the NZBs and Ragone plots

Figure S12 (a) Plots of log (i) vs log (v) of the NZBs according to the CV data at selected oxidation/reduction states. (b) Ragone plots of the aqueous NiMn-ZIF-S5//Zn battery based on the areal energy/power densities compared to other works.

Based on the power law relationship between peak current (i) and scan rate (v) to establish the equation[13]:

$$log\, i = b\, log\, v + log\, a$$

The *b*-value is usually between 0.5 and 1. When the *b*-value is close to the left endpoint the electrode reaction is controlled by capacitance, and close to the right extreme value the dynamics of the polar reaction is mainly a diffusion-controlled process. From Fig. S12a, the b-values of the two redox peaks are 0.80 and 0.96 respectively, which indicate that the capacitance control behavior is dominant[14].

The electrochemical performance of a complete battery can be foretold by qualitatively comparing the power and energy density calculated from cathode discharges under identical test conditions. In the Ragone plot (Fig. S12b), the surface energy/power densities of the present study are compared with those of other aqueous batteries which have been reported: the maximum surface energy density obtained by the NiMn-ZIF-S5//Zn cell at a power density of 0.64 mW cm^{-2} is 5.22 mWh cm^{-2}, and the maximum surface energy densities obtained by the other reported works such as CH@NC-LDH@NT//Zn@CC[15], Ni-NiO//Zn plate[16],

NiCo//Zn@Yarn[17], Ni-mMeSA//Zn@CC[8], NNA@CNH//NNA@Zn[18], VO_2-MWCHTs//Zn nanoflake[19].

14. XPS spectra after two-electrode system

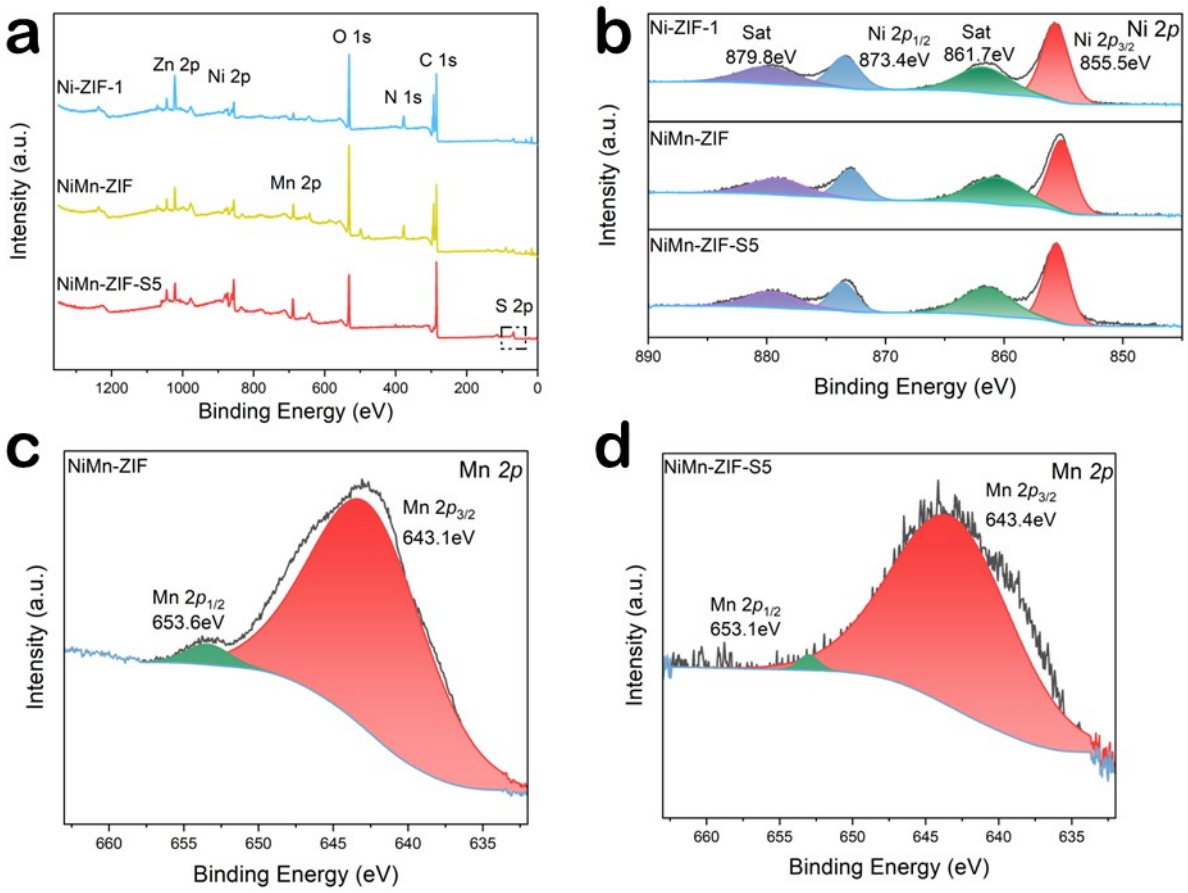

Figure S13. (a) Full XPS spectra, (b) Ni 2p, (c) Mn 2p and (f) S 2p XPS spectra of the Ni-ZIF-1, NiMn-ZIF and NiMn-ZIF-S5 after two-electrode system.

15. Contents of Ni and M elements in Ni-ZIF-X from ICP-OES.

Table S1. Contents of Ni and M elements in Ni-ZIF-X from ICP-OES.

Sample	Metal contents (mmol L^{-1})		Synthetic molar ratio	Atomic ratio in samples
	Ni	M		
Ni-ZIF-Al	0.902	0.014	Al /Ni=0.016	$Ni_1Al_{0.016}$
Ni-ZIF-Ag	/	0.692	/	/
NiCu-ZIF	2.03	0.039	Cu /Ni=0.019	$Ni_1Cu_{0.019}$
Ni-ZIF-Fe	1.08	0.041	Fe /Ni=0.037	$Ni_1Fe_{0.037}$
NiMn-ZIF	1.89	0.084	Mn/Ni=0.044	$Ni_1Mn_{0.044}$
NiZn-ZIF	1.82	0.081	Zn/Ni=0.044	$Ni_1Zn_{0.044}$

16. The surface areas and average pore diameters of Ni-ZIF-X.

Table S2. The surface areas and average pore diameters of Ni-ZIF-X.

Samples	Specific Surface Area (m^2/g)	Average Pore Diameter (nm)
Ni-ZIF-1	141.711	12.229
NiMn-ZIF	165.884	15.115
NiMn-ZIF-S5	54.64	16.660

17. Comparison of max. areal energy/power densities between our NiMn-ZIF-S5//Zn battery with other previously reported works.

Table S3. Comparison of max. areal energy/power densities between our NiMn-ZIF-S5//Zn battery with other previously reported works.

Samples	Max. EA (mWh cm^{-2})	Areal energy density at max. power density (mWh cm^{-2}/mW cm^{-2})		Refs
CH@NC-LDH@NT//Zn@CC	0.17	0.063	14.40	[15]
VO_2-MWCHTs//Zn nanoflake	0.189	0.072	0.61	[19]
NiCo//Zn@Yarn	0.120	0.054	32.80	[17]
Ni-mMeSA//Zn@CC	0.300	0.210	33.72	[8]
NNA@CNH//NNA@Zn	0.250	0.130	23.00	[18]
Ni-NiO//Zn plate	0.007	0.003	20.20	[16]
NiMn-ZIF-S5	**0.643**	**5.22**	**48.30**	**This work**

References

1. A. M. Kale, R. Manikandan, C. Justin Raj, A. Dennyson Savariraj, C. Voz and B. C. Kim, *Materials Today Energy*, 2021, **21**.
2. H. Guo, H. Zhang, N. Wu, Z. Pan, C. Li, Y. Chen, Y. Cao and W. Yang, *Journal of Alloys and Compounds*, 2023, **934**.
3. X. Wang, Y. Lin, Y. Su, B. Zhang, C. Li, H. Wang and L. Wang, *Electrochimica Acta*, 2017, **225**, 263-271.
4. F. Ji, J. Yu, S. Hou, J. Hu and S. Li, *Materials (Basel)*, 2024, **17**.
5. Y. Fazli, S. Mahdi Pourmortazavi, I. Kohsari and M. Sadeghpur, *Materials Science in Semiconductor Processing*, 2014, **27**, 362-367.
6. Y. Tang, J. Ding, W. Zhou, S. Cao, F. Yang, Y. Sun, S. Zhang, H. Xue and H. Pang, *Advanced Science*, 2023, **10**.
7. P. Vyawahare, H. Tun, M. W. Vaughn and C. C. Chen, *AIChE Journal*, 2021, **68**.
8. Y. Su, J. Hu, G. Yuan, G. Zhang, W. Wei, Y. Sun, X. Zhang, Z. Liu, N. T. Suen, H. C. Chen and H. Pang, *Advanced Materials*, 2023, **35**.
9. P. He, Y. Xie, Y. Dou, J. Zhou, A. Zhou, X. Wei and J.-R. Li, *ACS Applied Materials & Interfaces*, 2019, **11**, 41595-41601.
10. C. Yu, L. Zhang, J. Shi, J. Zhao, J. Gao and D. Yan, *Advanced Functional Materials*, 2008, **18**, 1544-1554.
11. Q. Wang, T. Liu, Y. Chen and Q. Wang, *Journal of Alloys and Compounds*, 2022, **891**.
12. S. Rajasekaran, B. S. Reghunath, S. D. K. R, B. Saravanakumar, J. Johnson William, D. Pinheiro and M. K. Arumugam, *Journal of Solid State Electrochemistry*, 2023, **27**, 911-925.
13. T. Chen, F. Wang, S. Cao, Y. Bai, S. Zheng, W. Li, S. Zhang, S. X. Hu and H. Pang, *Advanced Materials*, 2022, **34**.
14. Y. Su, G. Yuan, J. Hu, G. Zhang, Y. Tang, Y. Chen, Y. Tian, S. Wang, M. Shakouri and H. Pang, *Advanced Materials*, 2024, **36**.
15. Y. Wang, X. Hong, Y. Guo, Y. Zhao, X. Liao, X. Liu, Q. Li, L. He and L. Mai, *Small*, 2020, **16**.
16. Y. Zeng, Y. Meng, Z. Lai, X. Zhang, M. Yu, P. Fang, M. Wu, Y. Tong and X. Lu, *Advanced Materials*, 2017, **29**.
17. Y. Huang, W. S. Ip, Y. Y. Lau, J. Sun, J. Zeng, N. S. S. Yeung, W. S. Ng, H. Li, Z. Pei, Q. Xue, Y. Wang, J. Yu, H. Hu and C. Zhi, *ACS Nano*, 2017, **11**, 8953-8961.
18. C. Xu, J. Liao, C. Yang, R. Wang, D. Wu, P. Zou, Z. Lin, B. Li, F. Kang and C.-P. Wong, *Nano Energy*, 2016, **30**, 900-908.
19. J. Shi, S. Wang, X. Chen, Z. Chen, X. Du, T. Ni, Q. Wang, L. Ruan, W. Zeng and Z. Huang, *Advanced Energy Materials*, 2019, **9**.